

# Energy absorption of foam-filled lattice composite cylinders under lateral compressive loading

Jiye Chen<sup>1</sup>, Yong Zhuang<sup>2</sup>, Hai Fang<sup>\*1</sup>, Weiqing Liu<sup>\*\*3</sup>, Lu Zhu<sup>1</sup> and Ziyang Fan<sup>1</sup>

<sup>1</sup> College of Civil Engineering, Nanjing Tech University, Nanjing, China

<sup>2</sup> China Railway Major Bridge Reconnaissance & Design Institute Co., Ltd, Wuhan, China

<sup>3</sup> Advanced Engineering Composites Research Center, Nanjing Tech University, Nanjing, China

(Received March 14, 2018, Revised March 20, 2019, Accepted March 26, 2019)

**Abstract.** This paper reports on the energy absorption characteristics of a lattice-web reinforced composite sandwich cylinder (LRCSC) which is composed of glass fiber reinforced polymer (GFRP) face sheets, GFRP lattice webs, polyurethane (PU) foam and ceramsite filler. Quasi-static compression experiments on the LRCSC manufactured by a vacuum assisted resin infusion process (VARIP) were performed to demonstrate the feasibility of the proposed cylinders. Compared with the cylinders without lattice webs, a maximum increase in the ultimate elastic load of the lattice-web reinforced cylinders of approximately 928% can be obtained. Moreover, due to the use of ceramsite filler, the energy absorption was increased by 662%. Several numerical simulations using ANSYS/LS-DYNA were conducted to parametrically investigate the effects of the number of longitudinal lattice webs, the number of transverse lattice webs, and the thickness of the transverse lattice web and GFRP face sheet. The effectiveness and feasibility of the numerical model were verified by a series of experimental results. The numerical results demonstrated that a larger number of thicker transverse lattice webs can significantly enhance the ultimate elastic load and initial stiffness. Moreover, the ultimate elastic load and initial stiffness were hardly affected by the number of longitudinal lattice webs.

**Keywords:** cylinder; ceramsite filler; quasi-static compression; energy absorption; numerical simulation

## 1. Introduction

With the rapid development of waterborne transportation, problems associated with ships passing under bridges are becoming progressively serious, and ship-bridge collisions are increasing. The collisions may cause a great loss of lives as well as serious damage to the bridge (Perera and Soares 2005, Chai *et al.* 2017). Thus, improving the protection of bridge piers against ship collisions is of importance and has attracted increasing research attention.

After years of research and application, several types of anti-collision facilities have been developed based on the principle of energy absorption and momentum buffering, and each type of anti-collision facility has its own characteristics and operating conditions (Svensson 2009, Voyiadjis *et al.* 2008). Although steel fenders are more commonly used in China than other types of anti-collision facilities (Fan *et al.* 2015), the fender system has major drawbacks, such as high initial costs, poor corrosion resistance and high maintenance requirements (Jiang and Chorzepa 2015).

Composite sandwich structures are particularly appealing for anti-collision structures compared with traditional anti-collision facilities because of their enhanced

stability, higher strength to weight ratios, better energy absorption capacity and good cushioning performance (Azad and Ebrahimi 2016, Fan *et al.* 2014, Kafodya *et al.* 2015, Magnucki *et al.* 2014, Satasivam and Bai 2014, Satasivam *et al.* 2014, 2018, Taghipoor and Noori 2018, Yan and Song 2016, 2017, Yeganeh *et al.* 2016, Yurddaskal and Okutan Baba 2016, Xiao *et al.* 2018, Xie *et al.* 2014). Foam-filled sandwich panels composed of upper and lower face sheets and a polyurethane (PU) foam core were tested under quasi-static compression, and the results showed that the foam core plays an important role in energy absorption (Fang *et al.* 2010, Wu *et al.* 2014). However, foam-filled sandwich panels have low initial stiffness, low ultimate strength and severe interfacial debonding. Thus, a lattice-web reinforced composite sandwich panel was proposed to overcome these weaknesses, and such panel shows a significant increase in the ultimate bearing capacity under bending and compression because of the improved resistance to interfacial debonding between the face sheets and foam core (Wu *et al.* 2014, Wang *et al.* 2014, 2015). The lattice-web reinforced composite sandwich panel exhibits superior energy absorption capacity and is commonly used in anti-collision block forms for medium and small bridge collisions. However, it is difficult to manufacture large-scale lattice-web reinforced composite sandwich panels via the integral moulding method for direct use in large and medium bridge anti-collision facilities. Based on existing research of the lattice-web reinforced composite sandwich panel, Fang *et al.* (2016) proposed an innovative large-scale composite bumper system (LCBS)

\*Corresponding author, Professor,  
E-mail: fanghainjut@njtech.edu.cn

\*\*Co-corresponding author, Professor,  
E-mail: wqliu@njtech.edu.cn



(a) Panoramic view of Ma'anshan Yangtze River Bridge after the installation of the LCBS



(b) LCBS cylindrical segment

Fig. 1 Application of the LCBS for Ma'anshan Yangtze River Bridge

consisting of six or more large-scale cylindrical segments as bridge anti-collision facilities. The LCBS cylindrical segment, which using PU foam as the core and glass fiber-reinforced polymer (GFRP) as the face sheets and lattice webs, was manufactured through the vacuum-assisted resin infusion process (VARIP) method, which has been proved to be a feasible manufacturing method by a series of fabrication results (Fang *et al.* 2007). This novel anti-collision system presents several advantages, such as self-buoyancy in water, excellent corrosion resistance, modular segment fabrication, low maintenance requirements, and easy replacement of damaged segments, has already been installed on more than 10 bridges in China. The application of the LCBS for Ma'anshan Yangtze River Bridge is shown in Fig. 1. Thus, because of the advantages of this system, the energy absorption mechanism of the LCBS cylindrical segments has drawn research attention.

In this paper, the mechanical properties and energy absorption characteristics of a lattice-web reinforced composite sandwich cylinder (LRCSC) were investigated through experimental and numerical studies of lateral quasi-static compression. The LRCSC was manufactured through VARIP and loaded by pressing two rigid plates on the side of the cylinder. Parametric studies on the effects of the

number of longitudinal lattice webs, the number of transverse lattice webs, the thickness of transverse lattice webs and face sheets, and the inclusion of ceramsite filler in the cylinder were analysed. The failure modes, load-deflection curves and energy absorption capacities of the LRCSC with different lattice-web geometries and cylinder fillings were reported and discussed.

## 2. Materials and methods

### 2.1 Specimen description

In this study, eight LRCSCs were manufactured in the Advanced Composite Structures Research Center at Nanjing Tech University using the VARIP technique. All the cylinders had identical outer diameters ( $\Phi = 500$  mm), inner diameters ( $\phi = 300$  mm), lengths ( $L = 500$  mm), face sheet thicknesses ( $t_s = 2.4$  mm) and web thicknesses ( $t_w = 2.4$  mm), as listed in Table 1 and shown in Fig. 3(b). GFRP and HS-2101-G100 unsaturated polyester resin were used as the face sheets and webs. PU foam blocks with a nominal density of  $40 \text{ kg/m}^3$  were used to form the core. These blocks were bonded to the face sheets with the HS-2101-

Table 1 Details of the specimens

Specimen	$\Phi$ [mm] Outer diameter	$\phi$ [mm] Inner diameter	$L$ [mm] Length	$m$ [kg] Mass	Longitudinal lattice web		Transverse lattice web		Face-sheet thickness [mm]
					Number	Thickness [mm]	Number	Thickness [mm]	
D500-N*	500	300	500	10.01	—	—	—	—	2.4
D500-L8-T3	500	300	500	14.43	8	2.4	3	2.4	2.4
D500-L12-T4	500	300	500	16.41	12	2.4	4	2.4	2.4
D500-L16-T5	500	300	500	19.31	16	2.4	5	2.4	2.4
D500-N-C	500	300	500	30.35	—	—	—	—	2.4
D500-L8-T3-C	500	300	500	34.26	8	2.4	3	2.4	2.4
D500-L12-T4-C	500	300	500	36.79	12	2.4	4	2.4	2.4
D500-L16-T5-C	500	300	500	38.28	16	2.4	5	2.4	2.4

\* D500: outer diameter of the specimen is 500 mm; N: without lattice web; C: ceramsite filler; L8: number of longitudinal lattice webs is 8; and T3: number of transverse lattice webs is 3

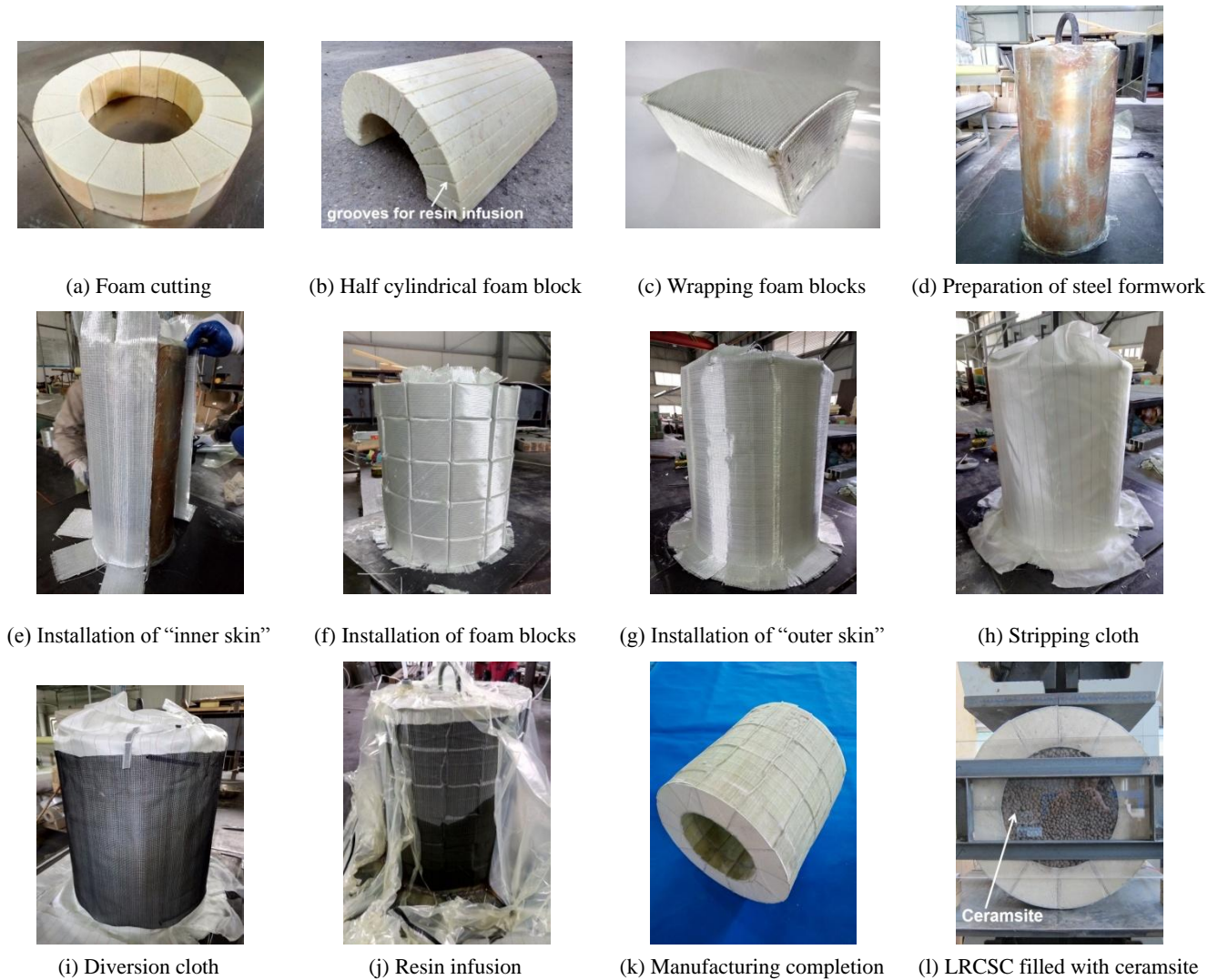


Fig. 2 Manufacturing process

G100 polyester resin mentioned above.

Eight specimens were divided into two groups, with each group containing four specimens. In one group (specimens D500-N-C, D500-L8-T3-C, D500-L12-T4-C, and D500-L16-T5-C), ceramsite with a nominal density of  $500 \text{ kg/m}^3$  was used to form the filler in the inner cylinder, whereas in the other group (specimens D500-N, D500-L8-T3, D500-L12-T4, and D500-L16-T5), ceramsite was not used. Table 1 gives the details of the specimens.

## 2.2 Process of manufacture

As shown in Fig. 2, a detailed illustration of the manufacture procedures of the LRCSC is divided into the following seven steps:

- (i) As shown in Fig. 2(a), the manufacture procedure began with the preparation of PU foam blocks, which were cut into annular sector cross-sections according to design dimensions. For specimens D500-N and D500-N-C whose cores were composed of two large-scale half cylindrical foam

blocks (Fig. 2(b)), many orthotropic grooves of approximately 2 mm in width and 3 mm in depth were predrilled on all the side faces for resin infusion during VARIP.

- (ii) As shown in Fig. 2(c), the foam blocks were wrapped by E-glass fiber mats with 2 layers of bi-axial [-45/45] glass fiber (weighing  $800 \text{ g/m}^2$  for each layer) to create the GFRP lattice webs. Several nail guns were used to hold the wrapped E-glass fiber mats in place.
- (iii) As shown in Fig. 2(d), a steel formwork in the shape of a circular cross-section was prepared. The side face of the steel formwork was covered with lithium grease. Then, the steel formwork was wrapped by a layer of plastic film to aid in the cylinder's removal.
- (iv) The installation of the “inner face sheet”, which consists of 2 layers of bi-axial [0/90] E-glass fiber mats (weighing  $800 \text{ g/m}^2$  for each layer), is shown in Fig. 2(e). Each layer was laid in a designated location to avoid overlapping the seams. Then, the PU foam blocks, which were wrapped with E-glass

fiber mats, were installed tightly in the formwork (Fig. 2(f)). Subsequently, the “outer face sheet”, which was also composed of 2 layers of bi-axial [45/45] E-glass fiber mats, was installed (Fig. 2(g)).

- (v) The formwork was then sealed by stripping cloth, diversion cloth and a vacuum bag for resin infusion as shown in Figs. 2(h), (i) and (j), respectively. The HS-2101-G100 unsaturated polyester resin was infused through the steel formwork by vacuum pressure using a series of predrilled ducts.
- (vi) After curing the resin for 8 h, the manufacture of the LRCSC was completed, as shown in Fig. 2(k).

- (vii) The LRCSC filled with ceramsite is shown in Fig. 2(l). To investigate the crushing process of ceramsite, two toughened glasses were used. More importantly, such two glasses were used to prevent the ceramsite particles from spilling out of the cylinder. A steel frame was used to fix the two toughened glasses.

Table 2 Material properties of the face sheets, foam and ceramsite

	Properties	Face sheets	PU foam	Ceramsite
Compression	Yield strength [MPa]	—	0.15	2.25
	Young’s modulus [MPa]	—	2.48	—
Tension	Yield strength [MPa]	322.90	—	—
	Young’s modulus [GPa]	20.08	—	—

2.3 Material properties

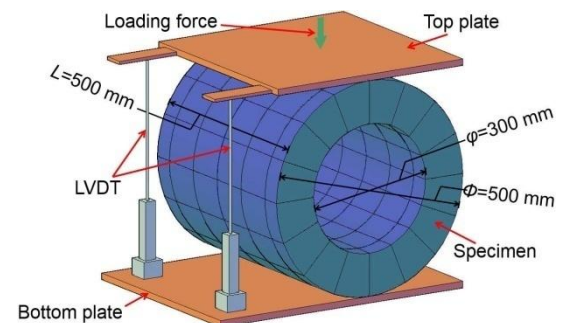
The tensile properties of the face sheets and webs were assessed under tensile tests according to ASTM D3039/D3039-14. Five tensile coupons with dimensions of 250 × 25 × 5 mm<sup>3</sup> were tested at a displacement rate of 2 mm/min until failure. The resulting tensile strength ranged from 305.2 MPa to 337.7 MPa, with an average of 322.9 MPa, and the resulting tensile elastic modulus ranged from 19.35 GPa to 20.50 GPa, with an average of 20.08 GPa. Table 2 gives an overview of the results.

The mechanical properties of the PU foam core were evaluated under compression with five cubic coupons of 50 × 50 × 50 mm<sup>3</sup>. The flatwise compression properties were determined according to ASTM C365-11 and conducted at a displacement rate of 0.5 mm/min. The ultimate compressive strength and compressive modulus were 0.15 MPa and 2.48 MPa, respectively. The properties of the PU foam are listed in Table 2.

The mechanical properties of the ceramsite, a type of coarse aggregate used to fill the inner cylinder, were

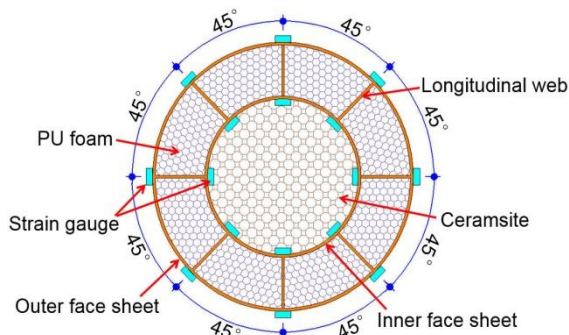


(a) Loading test set-up for specimen

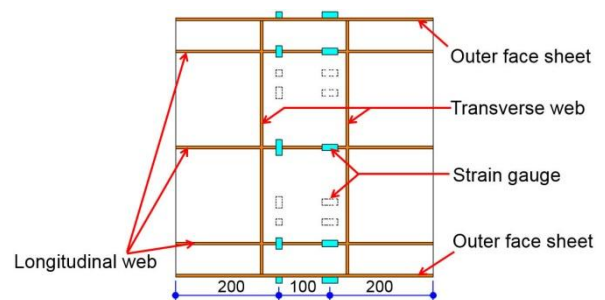


(b) Schematic representation

Fig. 3 Loading test set-up



(a) Planar view



(b) Side view

Fig. 4 Strain gauge arrangement (with total of 32 strain gauges)

determined according to ASTM C123/C123M-12 by testing five groups of ceramsite samples. The ceramsite samples were tested in a cylindrical testing vessel at a load rate of 300 N/min until the indentation depth reached 20 mm. The resulting cylindrical compressive strength ranged from 2.14 MPa to 2.41 MPa, with an average of 2.25 MPa, as listed in Table 2.

#### 2.4 Experimental set-up and instrumentation

Lateral compression tests were conducted on the cylinders according to ASTM D2412-11. The experimental set-up is shown in Fig. 3. All the experiments were performed on a universal testing machine with a maximum load capacity of 1000 kN, and the specimens were placed between two rigid plates during the lateral compression. The lateral compression tests were performed in a quasi-static condition with a loading rate of 2 mm/min.

To measure the vertical displacement in the testing process, each specimen was instrumented with two linear variable displacement transducers (LVDTs) with a stroke of 200 mm at the rigid support plate, as shown in Fig. 3. Up to thirty-two electric resistance strain gauges pasted on different cross-sections were adopted in the quasi-static compression tests. The readings of strain gauges were used to judge the failure modes and evaluate the performance of the cylinders. The arrangement of the strain gauges is shown in Fig. 4.

### 3. Experimental results and discussion

#### 3.1 Failure mode

The failure modes of all tested specimens can be categorized into three primary types: (1) PU foam core shear failure (Fig. 5(a)), which occurred in specimens D500-N and D500-N-C without lattice webs; (2) longitudinal lattice web delamination (Fig. 5(b)), which occurred in specimens D500-L8-T3, D500-L12-T4 and D500-L16-T5; (3) local buckling of the longitudinal lattice web (Fig. 5(c)), which was common in specimens D500-L8-T3-C, D500-L12-T3-C, and D500-L16-T5-C. The mechanisms that result in the corresponding failure modes can be explained as follows: (1) the maximum shear strain

of the foam core easily exceeded its ultimate strain due to the soft nature of PU foam; (2) the tensile stress in the interface was larger than the relatively low adhesive strength between the longitudinal lattice web and the PU foam core and delamination occurred between the longitudinal lattice web and the PU foam core; (3) the local compressive stress of the longitudinal lattice web reached the critical buckling stress before reaching the ultimate bending strength and then the local buckling of the longitudinal lattice web occurred. Unlike the cylinders (specimens D500-N and D500-N-C) without lattice web, the shear failure did not occur in the PU foam core due to the contribution of the webs, which improved the shear stiffness of the foam and provided resistance to the shear force. Compared with the specimens D500-L8-T3, D500-L12-T4 and D500-L16-T5, the delamination failure was not observed in specimens D500-L8-T3-C, D500-L12-T4-C and D500-L16-T5-C. This phenomenon can be explained by the presence of ceramsite, which improved the overall stiffness of the specimens and limited the interfacial tensile stress between the longitudinal lattice web and PU foam core.

#### 3.2 Load-deflection behaviour

##### 3.2.1 Load-deflection behavior of the test group without ceramsite filler

The load-deflection curves of the four cylinders without ceramsite filler, specimens D500-N, D500-L8-T3, D500-L12-T4 and D500-L16-T5, are shown in Fig. 6. Although all tests were conducted at a final displacement of 240 mm, the experimental phenomena indicated that all specimens could be completely collapsed at a displacement of 200 mm, therefore the displacement stage from 200 mm to 240 mm was not employed. Specimen D500-N exhibited two-phase behavior. In the first phase, up to approximately 15.04 kN (the ultimate elastic load), the behavior can be described as elastic and the initial stiffness was 0.62 kN/mm. In the second phase, the load-deflection curve showed yield behavior. A decrease in stiffness resulting from the onset of PU foam shear under shear stress was observed four times. The behavior of specimens D500-L8-T3, D500-L12-T4 and D500-L16-T5 was similar and can be described as four stages: (1) the elastic stage; (2) the decreasing stage; (3) the yield stage and (4) the hardening

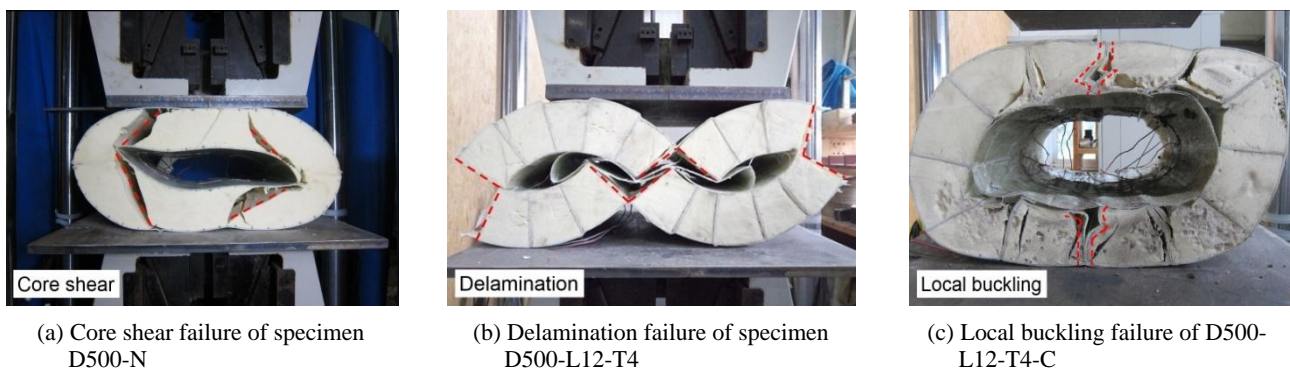


Fig. 5 Failure modes

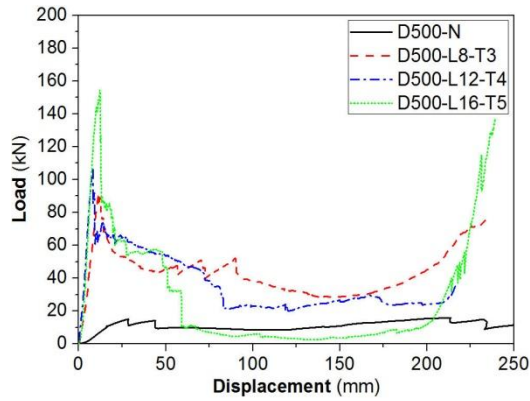


Fig. 6 Load-deflection curves of different cylinders without ceramsite filler

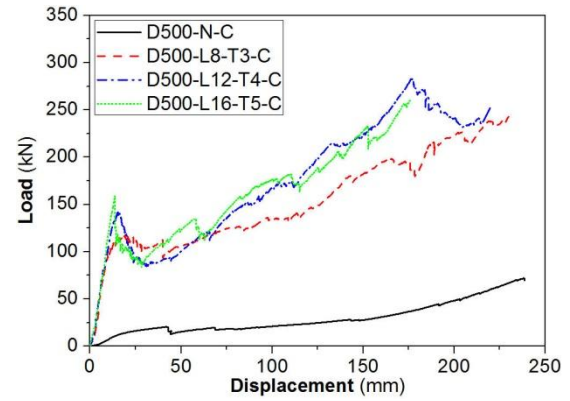


Fig. 7 Load-deflection curves of different cylinders with ceramsite filler

Table 3 Main experimental results

Specimen	Initial stiffness [kN/mm]	Ultimate elastic load [kN]	Failure mode
D500-N	0.62	15.04	Shear failure
D500-L8-T3	8.06	91.84	Delamination
D500-L12-T4	13.28	107.56	Delamination
D500-L16-T5	13.80	154.56	Delamination
D500-N-C	0.78	20.58	Shear failure
D500-L8-T3-C	9.78	118.74	Local buckling
D500-L12-T4-C	10.19	140.88	Local buckling
D500-L16-T5-C	11.62	159.16	Local buckling

stage. In the first stage, the three specimens D500-L8-T3, D500-L12-T4 and D500-L16-T5 displayed elastic behavior, and the initial stiffness values were 8.06 kN/mm, 13.28 kN/mm and 13.80 kN/mm, respectively, and the corresponding ultimate elastic loads were 91.84 kN, 107.50 kN and 154.56 kN, respectively. In the second stage, a sudden stiffness decrease was observed due to the delamination between the longitudinal lattice web and the PU foam. Subsequently, the stiffness underwent several changes, and then the cylinders entered the yield (third) stage. In the last stage, due to the PU foam gradually compacted under the compressive load, the specimens displayed hardening behavior and the bearing capacity continued to rise. The main experimental results are listed in Table 3.

Compared with specimen D500-N, specimens D500-L8-T3, D500-L12-T4 and D500-L16-T5 had a larger stiffness and ultimate elastic loads because of the reinforcement of the lattice webs used in the cylinder. As listed in Table 3, increasing the number of lattice webs can significantly improve the initial stiffness of the cylinders. Moreover, the ultimate elastic loads of the cylinders increased with the increase in the initial stiffness. Compared with the other three specimens (D500-N, D500-L8-T3, D500-L12-T4), specimen D500-L16-T5 had the maximum initial stiffness and ultimate elastic load but the minimum yield load of approximately 5 kN (3% of the ultimate elastic load), which was due to the enormous stiffness decrease leading to the

collapse of the cylinder. When specimen D500-L16-T5 was used as an anti-collision device, this collapse was disadvantageous because the enormous stiffness decrease was not conducive to energy absorption and the huge drop in bearing capacity over a very short time may cause secondary damage to people and impact objects.

### 3.2.2 Load-deflection behavior of the test group with ceramsite filler

The load-deflection responses of specimens D500-N-C, D500-L8-T3-C, D500-L12-T4-C and D500-L16-T5-C with ceramsite filler are shown in Fig. 7. The cylinders exhibited similar tri-linear behavior. In the first stage, the behavior can be described as elastic, and the initial stiffness values of specimens D500-N-C, D500-L8-T3-C, D500-L12-T4-C and D500-L16-T5-C were 0.78 kN/mm, 9.78 kN/mm, 10.19 kN/mm and 11.62 kN/mm, respectively, and the corresponding ultimate elastic loads were 20.58 kN, 118.74 kN, 140.88 kN and 159.16 kN, respectively, as listed in Table 3. In the second stage, the cylinders showed decreasing behavior, and the decreased stiffness was caused by the local buckling of the longitudinal lattice web. In the third stage, the bearing capacity continued to rise because of the ceramsite and the PU foam gradually compacted under the compressive load.

According to the values listed in Table 3, increasing the number of lattice webs can produce a larger initial stiffness, and then the ultimate elastic loads of the cylinders can be enhanced. As shown in Fig. 7, however, the rate of decline of the load-deflection curves decreased with the increase in the number of lattice webs. Hence, even if the initial stiffness of the cylinders was increased by increasing the number of lattice webs, poor ductility was observed.

### 3.2.3 Effect of ceramsite on load-deflection behaviour

The comparison of the load-deflection curves of cylinders with and without ceramsite is shown in Fig. 8. Compared with specimens D500-N and D500-L8-T3, the initial stiffness values of specimens D500-N-C and D500-L8-T3-C were increased by 25.8% and 21.3%, respectively. Moreover, the initial stiffness values of specimens D500-L12-T4-C and D500-L16-T5-C were approximately 23.3% and 15.8% smaller than those of specimens D500-L12-T4

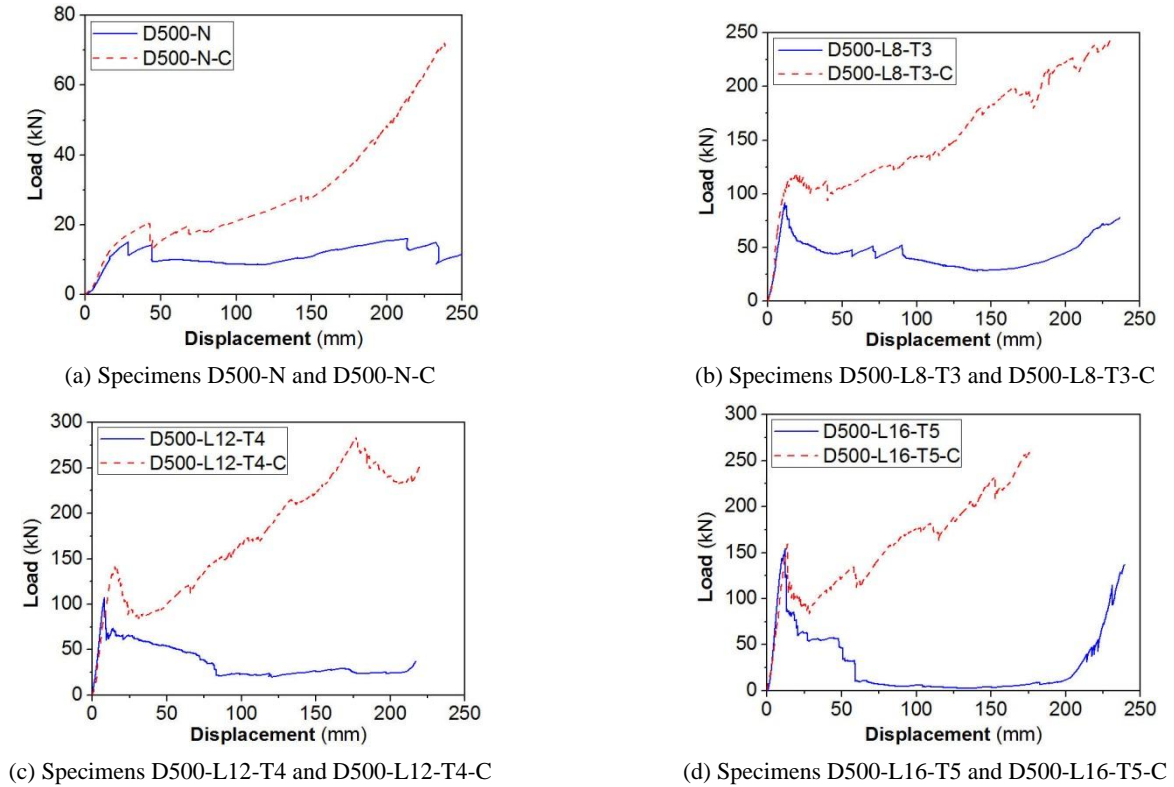


Fig. 8 Comparison of the load-deflection curves of different cylinders with and without ceramsite

Table 4 Energy absorption during compression

	Displacement [mm]	25	50	75	100	125	150	175	200
Energy absorption [J]	D500-N	178	486	731	958	1174	1425	1735	2095
	D500-L8-T3	1340	2515	3666	4770	5645	6385	7142	8102
	D500-L12-T4	1568	3028	4214	4871	5424	6027	6719	7328
	D500-L16-T5	1947	3345	3802	3938	4044	4123	4246	4460
	D500-N-C	219	654	1096	1577	2147	2815	3611	4667
	D500-L8-T3-C	2108	4728	7601	10805	14277	18484	23280	28424
	D500-L12-T4-C	2291	4572	7498	11277	15721	21044	27229	33695
	D500-L16-T5-C	2210	4826	8020	12077	16496	21595	27429	33998

and D500-L16-T5, respectively. Compared with specimens D500-N, D500-L8-T3, D500-L12-T4 and D500-L16-T5, the ultimate elastic loads of specimens D500-N-C, D500-L8-T3-C, D500-L12-T4-C and D500-L16-T5-C were increased by 36.8%, 29.3%, 31.0% and 3.0%, respectively. Throughout the testing process, the bearing capacity of specimens D500-N-C, D500-L8-T3-C, D500-L12-T4-C and D500-L16-T5-C was greater than that of specimens D500-N, D500-L8-T3, D500-L12-T4 and D500-L16-T5, respectively, due to the general bearing capacity enhanced by the ceramsite filler, as shown in Fig. 8. Moreover, the cylinders with ceramsite filler had better ductility than the cylinders without ceramsite filler, for the ceramsite improved the ductility of the cylinders and prevented the cylinders from breaking down. Compared with the cylinders without ceramsite filler, the cylinders with ceramsite filler had an excellent energy absorption capacity and can be

manufactured into anti-collision devices.

### 3.3 Discussion on energy absorption

#### 3.3.1 Energy absorption of the test group without ceramsite filler

To evaluate the energy absorption capacities of the cylinders, the energy absorption during testing,  $E$ , was considered and obtained by Eq. (1), as shown in Table 4.

$$E = \int_0^s F \cdot ds \quad (1)$$

where  $s$  and  $F$  are the compression-displacement and the corresponding load, respectively.

The cylinders with lattice webs exhibited a greater energy absorption capacity than the cylinders without lattice

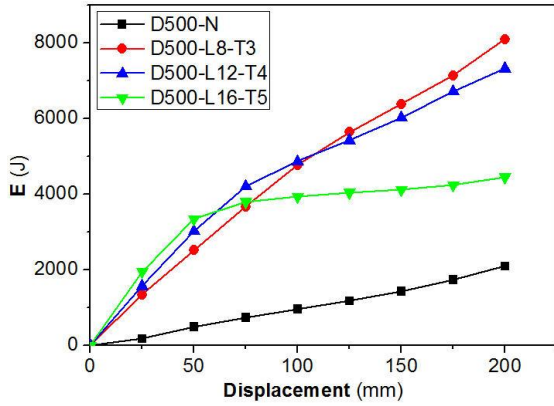


Fig. 9 Absorbed energy of different cylinders without ceramsite filler

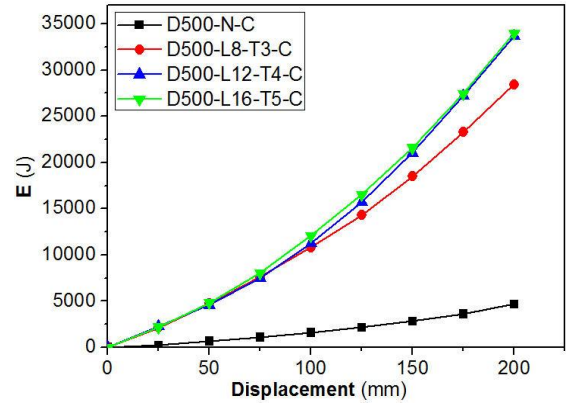


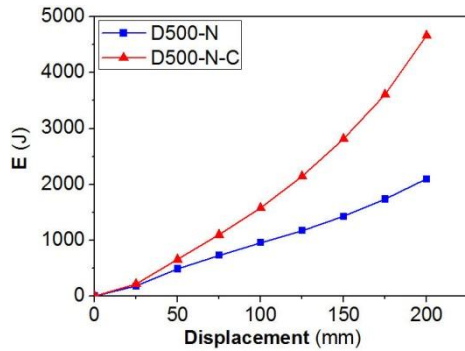
Fig. 10 Absorbed energy of different cylinders with ceramsite filler

webs (Figs. 9 and 10). In the liner elastic stage, the energy absorption capacity can be improved by increasing the number of lattice webs. At a displacement of 60 mm (approximately 40% of the final displacement), however, the energy absorption of specimen D500-L12-T4 was greater than the value of specimen D500-L16-T5. Moreover, at higher than 80 mm (approximately 33% of the final displacement) and 108 mm (approximately 45% of the final displacement), the energy absorption of specimens D500-L16-T5 and D500-L12-T4 was exceeded by specimen D500-L8-T3, respectively. The explanation for this phenomenon is that stiffer cylinders present an increased likelihood of brittle failure. As mentioned above,

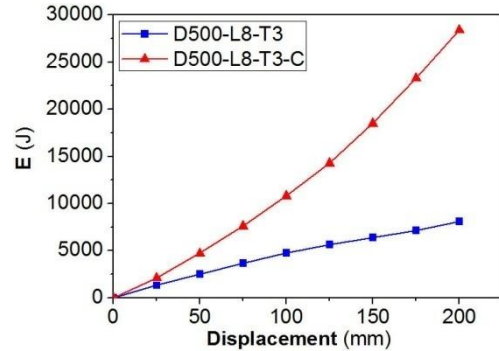
brittle failure caused the bearing load ( $F$ ) to decrease sharply and led to a decrease in energy absorption ( $E$ ).

### 3.3.2 Energy absorption of the test group with ceramsite filler

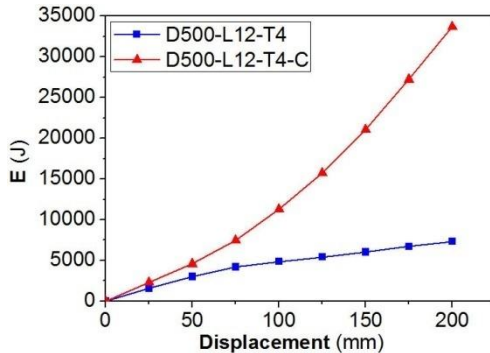
During testing, the energy absorption of specimens D500-L8-T3-C, D500-L12-T4-C and D500-L16-T5-C was over six times higher than that of specimen D500-N-C (Table 4). As shown in Fig. 10, the energy absorption was increased by increasing the number of lattice webs and due to the ductility of the cylinders being improved by the ceramsite filler, all curves grew steadily. Compared with specimen D500-L8-T3-C, specimen D500-L12-T4-C



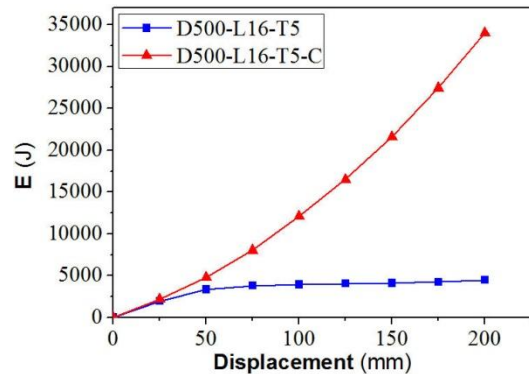
(a) Specimens D500-N and D500-N-C



(b) Specimens D500-L8-T3 and D500-L8-T3-C



(c) Specimens D500-L12-T4 and D500-L12-T4-C



(d) Specimens D500-L16-T5 and D500-L16-T5-C

Fig. 11 Comparison of the absorbed energy of different cylinders with and without ceramsite

exhibited a greater energy absorption capacity. However, the energy absorption curves of specimens D500-L12-T4-C and D500-L16-T5-C were nearly equivalent, which may have been related to the relative stiffness of the ceramsite filler compared with the lattice-web bracket. When the ceramsite filler and the lattice-web bracket shared similar stiffnesses, the cylinder exhibited a great energy absorption capacity.

### 3.3.3 Effect of ceramsite on energy absorption

The comparison of the energy absorption of cylinders with and without ceramsite is shown in Fig. 11. The cylinder with ceramsite filler had a greater energy absorption capacity than the cylinder without ceramsite filler, and the effect increased with an increase in compressive displacement. At a displacement of 200 mm (approximately 83% of the final displacement), the energy absorption of specimen D500-N-C was approximately twice as much as specimen D500-N, and the values of specimens D500-L8-T3-C, D500-L12-T4-C and D500-L16-T5-C were nearly two and a half times, three and a half times and six and a half times more than specimens D500-L8-T3, D500-L12-T4 and D500-L16-T5, respectively. Hence, the results indicate that the energy absorption capacity can be

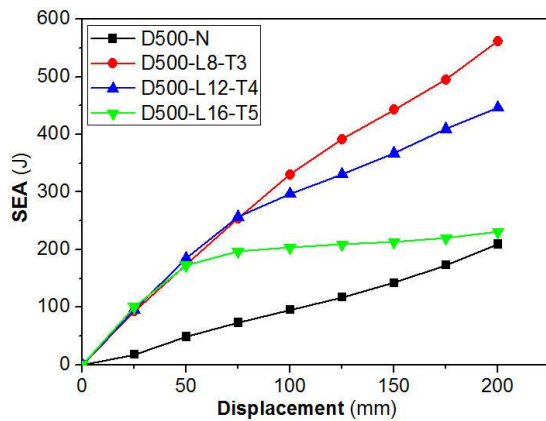


Fig. 12 Specific energy absorption of different cylinders without ceramsite filler

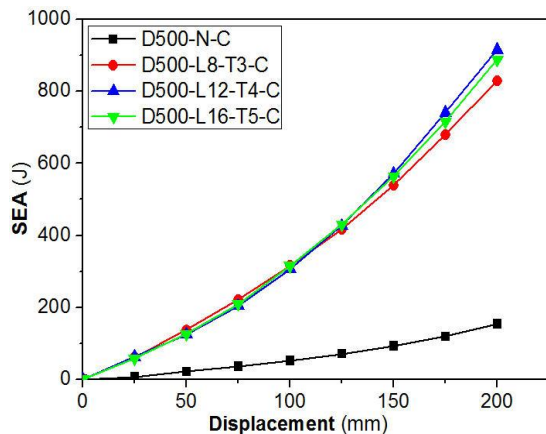


Fig. 13 Specific energy absorption of different cylinders with ceramsite filler

improved significantly by using ceramsite filler.

### 3.4 Specific energy absorption (SEA)

The specific energy absorption (*SEA*) describes the energy absorbed per unit mass and provides a method of comparing the energy absorption capacity of structures with different masses, and it is given by Eq. (2).

$$SEA = E/m \quad (2)$$

where  $m$  is the total mass of each specimen.

The *SEA* of the test groups without and with ceramsite are shown in Figs. 12 and 13, respectively. The cylinders using the lattice webs had a greater *SEA* capacity. In the elastic stage, the *SEA* capacity of each cylinder was nearly equivalent as shown in Fig. 12. Subsequently, compared with the other three cylinders, specimen D500-L8-T3 had a better *SEA* capacity when the displacement was above 75 mm. Throughout the entire test, the *SEA* capacities of specimens D500-L8-T3-C, D500-L12-T4-C and D500-L16-T5-C were nearly identical, as shown in Fig. 13.

The comparison of the *SEA* capacities of different cylinders is shown in Fig. 14. Due to the large mass of ceramsite, the *SEA* capacity of specimen D500-N-C was always lower than specimen D500-N. In the elastic stage, the cylinders without ceramsite filler exhibited greater *SEA* capacities than the cylinders with ceramsite filler. When the displacements were approximately 100 mm, 100 mm and 75 mm, the *SEA* capacities of specimens D500-L8-T3-C, D500-L12-T4-C and D500-L16-T5-C exceeded those of specimens D500-L8-T3, D500-L12-T4 and D500-L16-T5, respectively, which was due to the energy absorption of the ceramsite.

### 3.5 Mean crushing load (MCL)

One of the most significant parameters for quantifying the behavior of lateral compressed cylinders is the mean crushing load (*MCL*), which is obtained by dividing the measured absorbed energy by the crushing distance  $S$ .

$$MCL = E/S \quad (3)$$

where  $S$  is the compression-displacement of each specimen.

The *MCLs* of the four cylinders without ceramsite filler are shown in Fig. 15. At the beginning of the experiment, the *MCL* of specimen D500-N rose to a value of approximately 10 kN and then remained essentially constant. The *MCLs* of the other three cylinders continued decreasing throughout the test, especially for specimen D500-L16-T5. The *MCL* of specimen D500-L8-T3, however, decreased slowly with the increase in displacement and exceeded that of specimens D500-L12-T4 and D500-L16-T5 at displacements of approximately 100 mm and 75 mm, respectively.

The *MCLs* of the four cylinders with ceramsite filler are shown in Fig. 16. In this test group, the *MCLs* of the cylinders without lattice webs were much less than those of the cylinders with lattice webs, and up to a displacement of approximately 75 mm, the *MCL* increased with the increase in the number of lattice webs. Compared with specimen

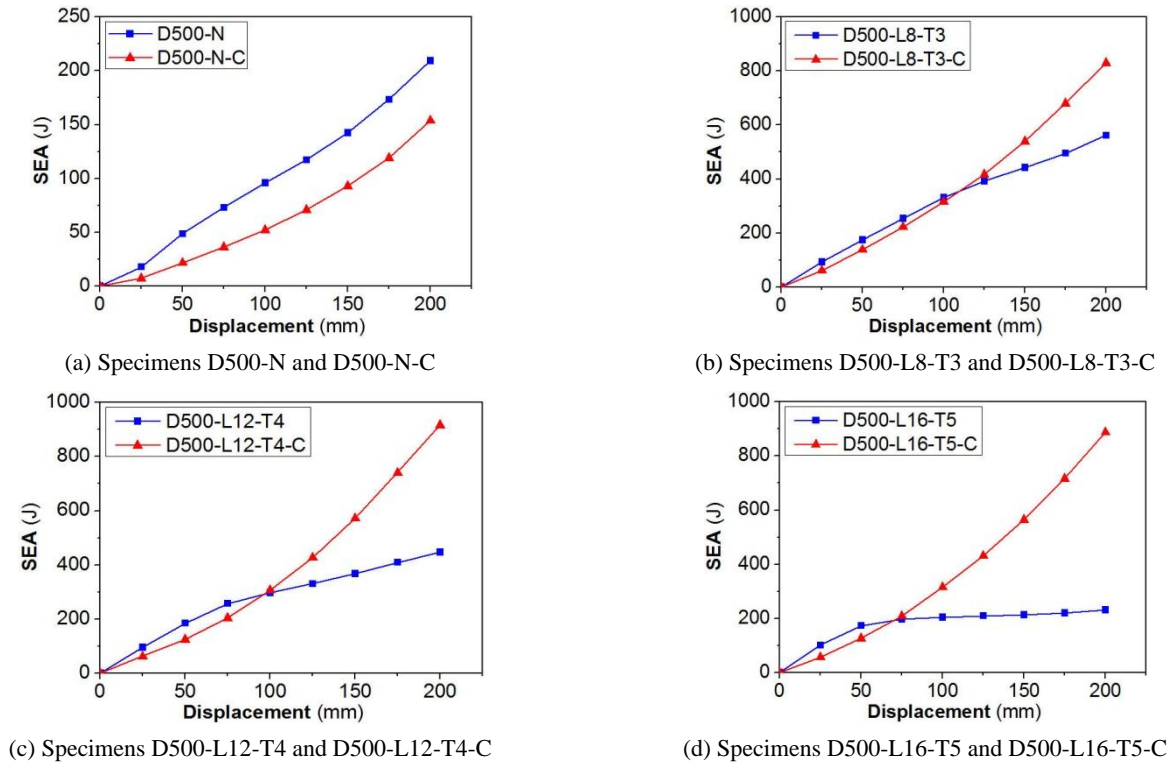


Fig. 14 Comparison of the SEA of different cylinders with and without ceramsite

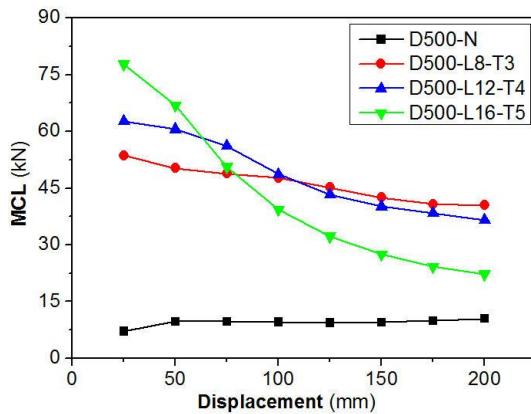


Fig. 15 Mean crushing load of different cylinders without ceramsite filler

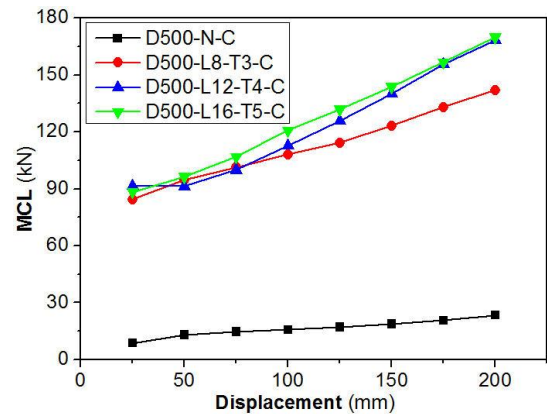


Fig. 16 Mean crushing load of different cylinders with ceramsite filler

D500-L16-T5-C, the MCL of specimen D500-L12-T4-C increased by no more than 7 percent. Hence, the MCLs of the cylinders were not always obviously improved by increasing the number of lattice webs, although the relative stiffness of the ceramsite filler compared with the lattice-web bracket may have been improved.

The comparison of the MCLs of the cylinders with and without ceramsite filler is shown in Fig. 17. The MCLs of the cylinders were improved by the use of ceramsite filler. When the displacement was 100 mm, the MCLs of specimens D500-L8-T3-C, D500-L12-T4-C and D500-L16-T5-C were twice as high as those of specimens D500-L8-T3, D500-L12-T4 and D500-L16-T5, respectively. The MCLs of the cylinders with ceramsite filler increased gradually with the increase of displacement.

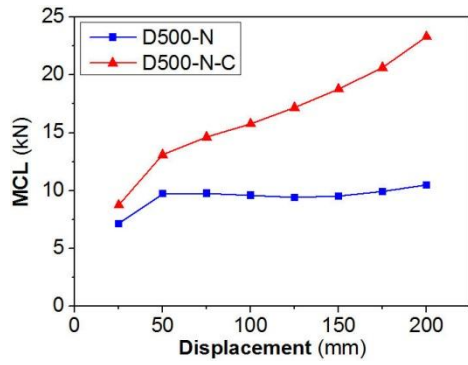
## 4. Finite element modelling

### 4.1 Modelling details

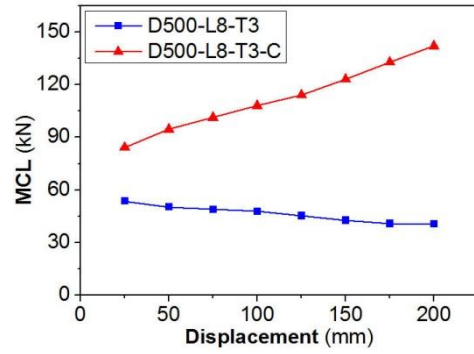
The nonlinear explicit finite element (FE) code ANSYS/LS-DYNA is used to simulate the large deformation and energy absorption capacity of the LRCSC subjected to quasi-static lateral compression. As shown in Fig. 18, in this model, two rigid plates consisting of movable rigid and constrained rigid plates are placed on the top and the bottom of the LRCSC, respectively.

#### 4.1.1 Element type

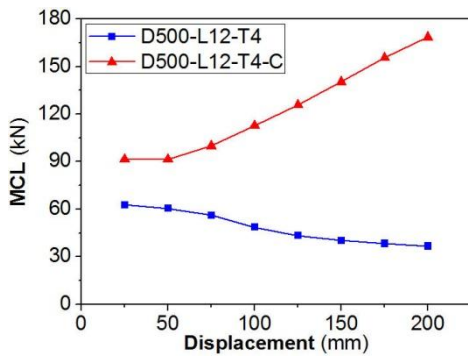
In the present study, the inner and outer face sheets and the lattice webs were modelled using 4-node shell elements,



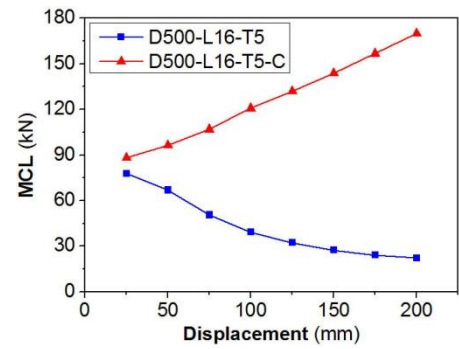
(a) Specimens D500-N and D500-N-C



(b) Specimens D500-L8-T3 and D500-L8-T3-C

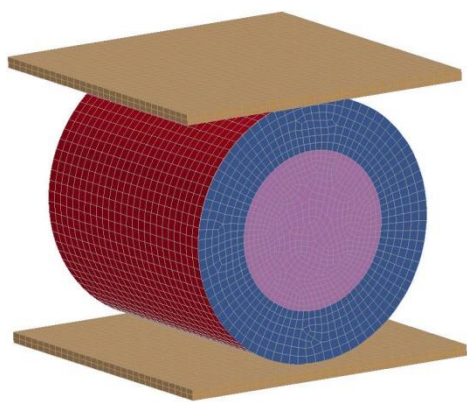


(c) Specimens D500-L12-T4 and D500-L12-T4-C

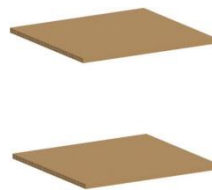


(d) Specimens D500-L16-T5 and D500-L16-T5-C

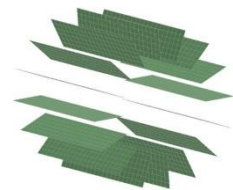
Fig. 17 Comparison of the MCL of different cylinders with and without ceramsite



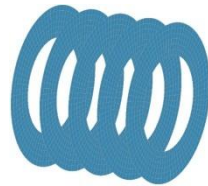
(a) Specimen D500-L16-T5



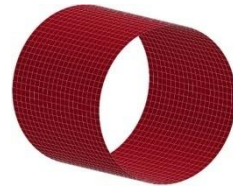
(c) Rigid plates



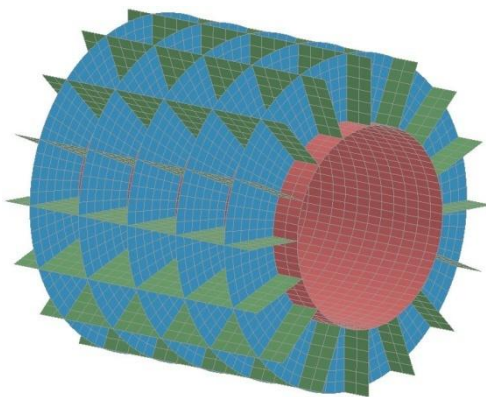
(d) Longitudinal lattice webs



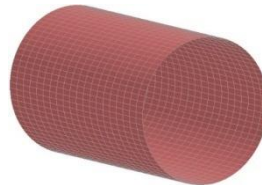
(e) Transverse lattice webs



(f) Outer face sheet



(b) Lattice webs and inner face sheet



(g) Inner face sheet



(h) PU foam



(i) Ceramsite filler (optional)

Fig. 18 Model geometry

Table 5 Material parameters of the GFRP face sheets and lattice webs

$\rho$ [g/cm <sup>3</sup> ]	$E_x$ [GPa]	$E_y$ [GPa]	$E_z$ [GPa]	$G_{xy}$ [GPa]	$G_{xz}$ [GPa]	$G_{yz}$ [GPa]	
1.8	20.0	20.0	6.67	2.5	1.25	1.25	
$NU_{xy}$	$NU_{xz}$	$NU_{yz}$	$S_c$ [MPa]	$X_t$ [MPa]	$Y_t$ [MPa]	$Y_c$ [MPa]	$\alpha$
0.15	0.1	0.1	55.0	322.9	322.9	168.2	0.3

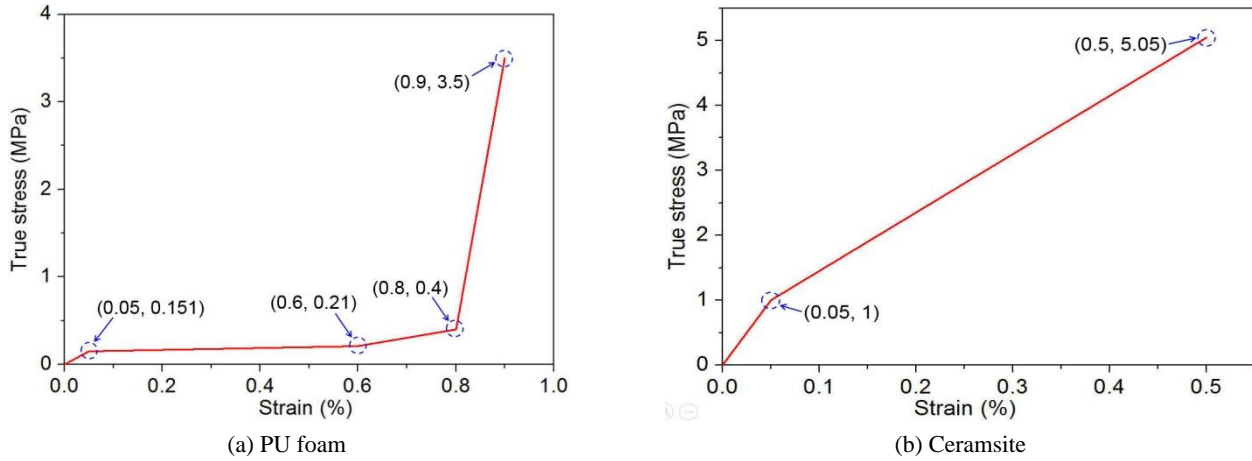


Fig. 19 True stress-strain curves

SHELL163, with 5-integration points through thickness, which was formulated by Belytschko *et al.* (1984). This formulation is extensively used by the researchers in thin-walled cylinder applications as a result of its efficiency, utilizing a reduced integration scheme. The foam filling, the ceramsite filler and the moving and supporting rigid plates were discretized with 8-node brick element, SOLID164, which was implemented with the reduced integration technique and used in combination with an hourglass control. The mesh size was controlled by the element size of the line segment, and each model was kept the same mesh size as shown in Fig. 18. The inner core, as shown in Fig. 18(i), was only established for specimens with ceramsite filler. To identify the optimum mesh size, the mesh was successively refined.

4.1.2 Material model

A composite damage model is used to model the GFRP face sheets and lattice webs. The orthotropic material with optional brittle failure for composites can be defined

following the suggestion of Chang (Chang and Chang 1987a, b). Table 5 lists the parameters for GFRP face sheets and lattice webs based on the composite damage model. The crushable foam model, which is dedicated to modelling crushable foam with optional damping and tension cut-off, is used to model the PU foam and ceramsite filler. The true stress-strain curves for both the PU foam and ceramsite filler are used to introduce the approximated true stress-strain data points in the numerical simulation. The approximated true stress-strain curves for the PU foam and ceramsite filler used in the FE modes are shown in Figs. 19(a) and (b), respectively. Moreover, a failure criterion is applied to the crushable foam model, and the element will be deleted from the calculation when the shear strain reaches 0.1.

4.1.3 Load and boundary conditions

The quasi-static load is simulated by moving the top rigid plate with a constant downward velocity. The bottom rigid plate was constrained in all translational degrees of



Fig. 20 Crushed shape of specimen D500-L16-T5

freedom, and the top rigid plate was fixed in all translational degrees of freedom except the vertical displacement with a constant rate of 2 mm/min. An ‘automatic surface to surface’ contact with a coefficient of friction of 0.2 suggested by Yin *et al.* (2014) and Zhang *et al.* (2018) was selected to define the contact among the movable rigid plate, the constrained rigid plate and the specimen.

#### 4.1.4 Quasi-static simulation

In the explicit FE method, the selected time step is usually very small to maintain numerical stability. The minimum stable time step in the explicit analysis is determined by the characteristic element length, Young’s modulus, and material density. However, such a small time step is inappropriate for quasi-static deformation because many steps are required for the quasi-static simulation. The computational time has commonly been minimized using two approaches: (1) scale up the mass density and/or (2) scale up the deformation velocity (Yazdani Sarvestani *et al.* 2019). In the present study, the actual velocity of 2 mm/min is scaled up to 100 mm/s. Since the calculated kinetic energy is 1.4% of the total internal energy over the period of the crushing process, such an approach has achieved a quasi-static process.

#### 4.2 Validation of the numerical simulations

The main objective of the validation study was to show that the response of the test specimens could be predicted by numerical models with sufficient accuracy. The FE

model for lateral quasi-static compressive loading was validated by comparing the predicted deformation mode and load-deflection with the experimental results.

As shown in Fig. 20, the final crushed shape of specimen D500-L16-T5 under lateral quasi-static compressive loading compared with the experimental observation indicated that FE modelling can simulate the deformation of the cylinder with sufficient accuracy.

For the purpose of verification, specimens D500-L8-T3, D500-L12-T4, D500-L8-T3-C and D500-L12-T4-C were also simulated and then compared with the experimental tests. The comparison of the load-deflection curves between the experimental and numerical simulation is shown in Fig. 21. The numerical curve successfully produced the crushing behavior, although only a slight difference was observed between the predicted load and the experimental results in the plastic stage because many unknowns are associated with the interaction among the GFRP, the PU foam and the ceramsite filler and have not been completely described in the models. Considering the complexity of the components in the cylinder, the comparison indicated that the FE model can simulate the response of the test specimen reasonably well.

### 5. Parametric study

The numerical static load-deflection curves are presented along with a discussion on the effect of various parameters on the crush response of the LRCSC.

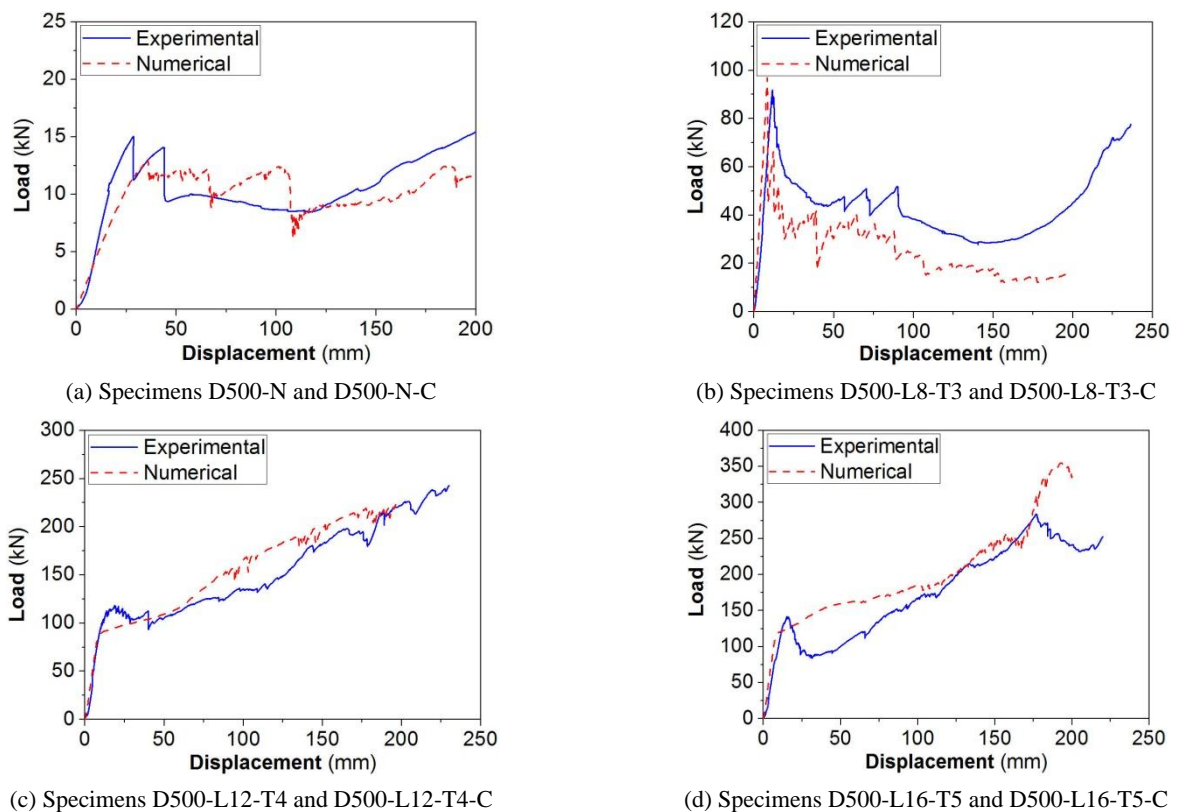


Fig. 21 Comparison of experimental and numerical static load-deflection curves of four different cylinders

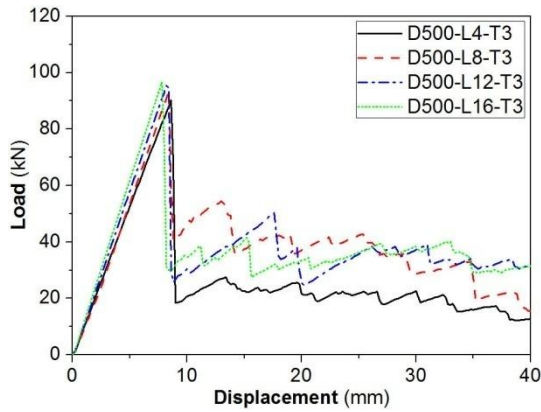


Fig. 22 Load-deflection curves of cylinders with different numbers of longitudinal lattice webs

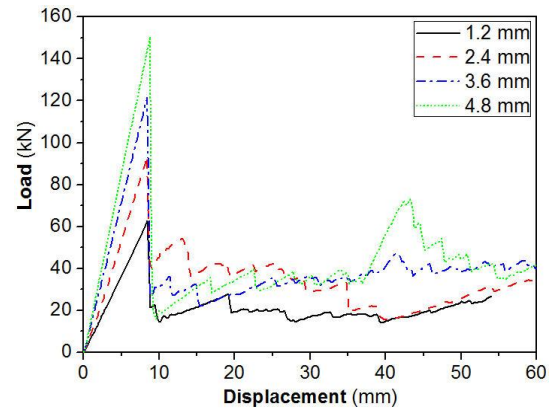


Fig. 24 Load-deflection curves of cylinders with different transverse lattice-web thicknesses

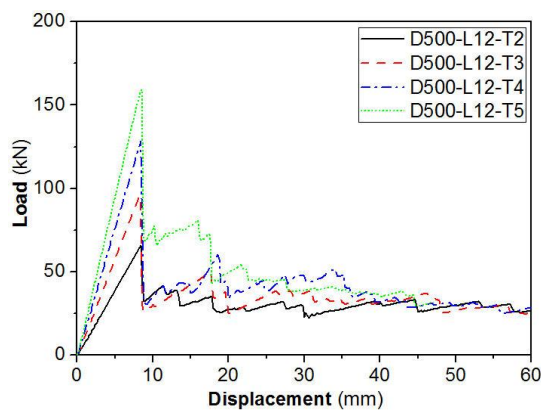


Fig. 23 Load-deflection curves of cylinders with different numbers of transverse lattice webs

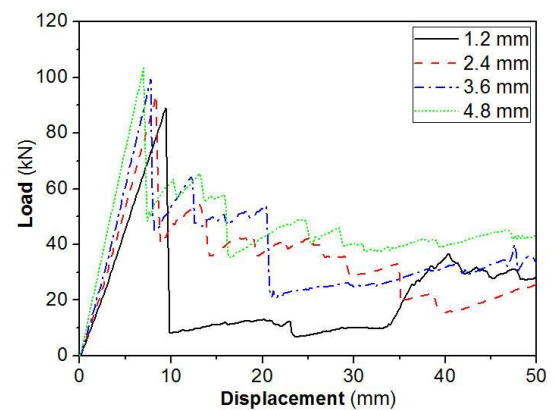


Fig. 25 Load-deflection curves of cylinders with different GFRP face-sheet thicknesses

### 5.1 Effect of the number of longitudinal lattice webs

In the numerical simulation, four different numbers of longitudinal lattice webs (4, 8, 12 and 16) were simulated. To provide a meaningful comparison, the number of transverse lattice webs was kept the same (3). As shown in Fig. 22, the number of longitudinal lattice webs does not change the ultimate elastic load and initial stiffness level. The ultimate elastic loads of specimens D500-L4-T3, D500-L8-T3, D500-L12-T3 and D500-L16-T3 were 90.28 kN, 93.53 kN, 95.41 kN and 96.59 kN, respectively, and the corresponding initial stiffness values were 10.50 kN/mm, 11.13 kN/mm, 11.64 kN/mm and 12.38 kN/mm, respectively. The differences in the ultimate elastic load and initial stiffness among these four cylinders were negligible. Hence, the ultimate elastic load and initial stiffness were hardly affected by the number of longitudinal lattice webs.

### 5.2 Effect of the number of transverse lattice webs

Four different numbers of transverse lattice webs (2, 3, 4 and 5) were adopted to investigate the effect of the number of transverse lattice webs on the ultimate elastic load and initial stiffness. The number of longitudinal lattice webs was kept at a constant value of 12 to provide a meaningful comparison. As shown in Fig. 23, increasing the number of

transverse lattice webs can significantly improve the ultimate elastic load and initial stiffness. The ultimate elastic loads of specimens D500-L12-T2, D500-L12-T3, D500-L12-T4 and D500-L12-T5 were 65.80 kN, 95.41 kN, 128.42 kN and 159.16 kN, respectively, and the corresponding initial stiffness values were 7.83 kN/mm, 11.64 kN/mm, 15.29 kN/mm and 18.51 kN/mm, respectively. The ultimate elastic load and initial stiffness of specimen D500-L12-T5 were both nearly two and a half times greater than that of specimen D500-L12-T3. Hence, increasing the number of transverse lattice webs can obtain a larger initial stiffness, and then the ultimate elastic load of a cylinder can be improved.

### 5.3 Effect of the transverse lattice-web thickness

As shown in Fig. 24, the effect of the transverse lattice-web thickness on the ultimate elastic load and initial stiffness under the same number of longitudinal lattice webs (8) and transverse lattice webs (3) was provided. The ultimate elastic load and initial stiffness increased with the increase in the transverse lattice-web thickness. When the transverse lattice-web thicknesses were 1.2 mm, 2.4 mm, 3.6 mm and 4.8 mm, the ultimate elastic loads of specimen D500-L8-T3 were 62.66 kN, 93.53 kN, 121.54 kN and 150.65 kN, respectively, and the corresponding initial

stiffness values were 7.46 kN/mm, 11.13 kN/mm, 14.47 kN/mm and 17.12 kN/mm, respectively. Compared with specimen D500-L8-T3, which had a transverse web thickness of 1.2 mm, the ultimate elastic load and initial stiffness of specimen D500-L8-T3, which had a transverse web thickness of 4.8 mm, increased by 145.1% and 129.5%, respectively. Therefore, using thicker transverse lattice webs can significantly increase the ultimate elastic load and initial stiffness.

#### 5.4 Effect of the GFRP face-sheet thickness

As shown in Fig. 25, the effect of the GFRP face-sheet thickness on the ultimate elastic load and initial stiffness under the same number of longitudinal lattice webs (8) and transverse lattice webs (3) was provided. When the GFRP face-sheet thicknesses were 1.2 mm, 2.4 mm, 3.6 mm and 4.8 mm, the ultimate elastic loads of specimen D500-L8-T3 were 89.03 kN, 95.53 kN, 99.54 kN and 103.39 kN, respectively, and the corresponding initial stiffness values were 9.47 kN/mm, 11.13 kN/mm, 12.76 kN/mm and 14.77 kN/mm, respectively. Compared with specimen D500-L8-T3, which had a face-sheet thickness of 1.2 mm, the ultimate elastic load and initial stiffness of specimen D500-L8-T3, which had a face-sheet thickness of 4.8 mm, increased by 16.1% and 60.0%, respectively. Therefore, the initial stiffness increased to some extent with the increase in the GFRP face-sheet thickness, although a corresponding increase in the ultimate elastic load was not observed.

## 6. Conclusions

This paper presented the crush behavior and energy absorption of the LRCSC under lateral quasi-static compression loading. The numerical simulation has indicated that the overall behavior of the crushing process follows the actual test condition. The main findings of the present experimental and numerical studies can be summarized as follows:

- The experimental results showed that a maximum increase in the ultimate elastic load of the LRCSC of approximately 928% can be obtained via the enhancement of lattice webs compared with the cylinders without lattice webs.
- The energy absorption, specific energy absorption and mean crushing load were determined by the failure mode. The cylinder that presented brittle failure because of the large stiffness value caused by the excessive lattice-web bracket showed poor energy absorption capacity. Thus, an appropriate number of lattice webs should be selected to obtain a good energy absorption capacity.
- In the crushing process, ceramsite filler played an important role in energy absorption. Thus, due to the use of ceramsite filler, the ultimate elastic load and energy absorption were increased by approximately 36.8% and 662%, respectively.
- The numerical model based on the material properties and failure modes obtained from

experimental investigations could well predict the crush response. The parametric study based on the validated numerical model indicated that the thicker and larger number of transverse lattice webs can significantly enhance the ultimate elastic load and initial stiffness of the LRCSC. In addition, an increase of the GFRP face-sheet thickness could increase the initial stiffness to some extent. However, the number of longitudinal lattice webs only had a slight effect on the ultimate elastic load and initial stiffness.

## Acknowledgments

The research described herein was supported by the National Natural Science Foundation of China (Grant No. 51578285 and 51778285) and the Natural Science Foundation of Jiangsu Province (Grant No. BK20161545).

## References

- Azad, N.V. and Ebrahimi, S. (2016), "Energy absorption characteristics of diamond core columns under axial crushing loads", *Steel Compos. Struct., Int. J.*, **21**(3), 605-628.
- Belytschko, T., Lin, J.I. and Tsay, C.S. (1984), "Explicit algorithms for the nonlinear dynamics of shells", *Comput. Method. Appl. M.*, **42**(2), 225-251.
- Chai, T., Weng, J.X. and Xiong, D. (2017), "Development of a quantitative risk assessment model for ship collisions in fairways", *Safety Sci.*, **91**, 71-83.
- Chang, F.K. and Chang, K.Y. (1987a), "Post-failure analysis of bolted composite joints in tension or shear-out mode failure", *J. Compos. Mater.*, **21**(9), 809-833.
- Chang, F.K. and Chang, K.Y. (1987b), "A progressive damage model for laminated composites containing stress concentrations", *J. Compos. Mater.*, **21**(9), 834-855.
- Fan, X.M., Wang, L., Liu, W.Q. and Chen, H. (2014), "Energy-absorption properties of foam-filled GFRP circular cylinders under compression loading", *Fiber Reinf. Plast./Compos.*, **12**, 36-40.
- Fan, W., Yuan, W.C. and Chen, B.S. (2015), "Steel fender limitations and improvements for bridge protection in ship collisions", *J. Bridge Eng.*, **20**(12).  
DOI: 10.1061/(ASCE)BE.1943-5592.0000785
- Fang, H., Liu, W.Q. and Wan, L. (2007), "Mechanical properties of innovative sandwich composites fabricated by vacuum infusion molding process", *J. Cent. South Univ. Technol.*, **14**, 7-11.
- Fang, H., Liu, W.Q., Lu, W.D. and Wan, L. (2010), "Flexural properties of grooved perforation sandwich composites", *J. Wuhan Univ. Technol.*, **25**(4), 583-587.
- Fang, H., Mao, Y.F., Liu, W.Q., Zhu, L. and Zhang, B. (2016), "Manufacturing and evaluation of Large-scale Composite Bumper System for bridge pier protection against ship collision", *Compos. Struct.*, **158**, 187-198.
- Jiang, H. and Chorzepa, M.G. (2015) "Evaluation of a new FRP fender system for bridge pier protection against vessel collision", *J. Bridge Eng.*, **20**(2).  
DOI: 10.1061/(ASCE)BE.1943-5592.0000658
- Kafodya, I., Xian, G.J. and Li, H. (2015), "Durability study of pultruded CFRP plates immersed in water and seawater under sustained bending: Water uptake and effects on the mechanical properties", *Compos.: Part B*, **70**, 138-148.

- Magnucki, K., Jasion, P., Szyk, W. and Smyczynski, M. (2014), "Strength and buckling of a sandwich beam with thin binding layers between faces and a metal foam core", *Steel Compos. Struct., Int. J.*, **16**(3), 325-337.
- Perera, L.P. and Soares, C.G. (2005), "Collision risk detection and quantification in ship navigation with integrated bridge systems", *Ocean Eng.*, **109**, 344-354.
- Santosa, S.R., Wierzbicki, T., Hanssen, A.G. and Langseth, M. (2000), "Experimental and numerical studies of foam-filled sections", *Int. J. Impact Eng.*, **24**(5), 509-534.
- Satasivam, S. and Bai, Y. (2014), "Mechanical performance of bolted modular GFRP composite sandwich structures using standard and blind bolts", *Compos. Struct.*, **117**, 59-70.
- Satasivam, S., Bai, Y. and Zhao, X.L. (2014), "Adhesively bonded modular GFRP web-flange sandwich for building floor construction", *Compos. Struct.*, **111**, 381-392.
- Satasivam, S., Bai, Y., Yang, Y., Zhu, L. and Zhao, X.L. (2018), "Mechanical performance of two-way modular FRP sandwich slabs", *Compos. Struct.*, **184**, 904-916.
- Song, H.W., Wan, Z.M. and Du, X.W. (2002), "Microscopic mechanism of energy absorption behavior for glass/epoxy cylinders under impact loading", *Acta Mater. Compos. Sin.*, **19**(2), 75-79.
- Svensson, H. (2009), "Protection of bridge piers against ship collision", *Steel Constr.*, **2**(1), 21-32.
- Taghipoor, H. and Noori, M.D. (2018), "Experimental and numerical study on energy absorption of lattice-core sandwich beam", *Steel Compos. Struct., Int. J.*, **27**(2), 135-147.
- Voyiadjis, G.Z., El-Tawil, S.M. and Kocke, P.J. (2008), *Feasibility of tubular fender units for pier protection against vessel collision*, Louisiana Transportation Research Center, Baton Rouge, LA, USA.
- Wang, L., Liu, W.Q., Wan, L., Fang, H. and Hui, D. (2014), "Mechanical performance of foam-filled lattice composite panels in four-point bending: experimental investigation and analytical modeling", *Compos.: Part B*, **67**, 270-279.
- Wang, L., Liu, W.Q., Fang, H. and Wan, L. (2015), "Behavior of sandwich wall panels with GFRP face sheets and a foam-GFRP web core loaded under four-point bending", *J. Compos. Mater.*, **49**(22), 2765-2778.
- Whitney, M.W., Harik, I.E., Griffin, J.J. and Allen, D.L. (1996), "Barge collision design of highway bridges", *J. Bridge Eng.*, **1**(2), 47-58.
- Wu, Z.M., Liu, W.Q., Wang, L., Fang, H. and Hui, D. (2014), "Theoretical and experimental study of foam-filled lattice composite panels under quasi-static compression loading", *Compos.: Part B*, **60**, 329-340.
- Xiao, W., Yan, C., Tian, W.B., Tian, W.P. and Song, X.D. (2018), "Effects of face-sheet materials on the flexural behavior of aluminum foam sandwich", *Steel Compos. Struct., Int. J.*, **29**(3), 301-308.
- Xie, Z.H., Yan, Q. and Li, X. (2014), "Investigation on low velocity impact on a foam core composite sandwich panel", *Steel Compos. Struct., Int. J.*, **17**(2), 159-172.
- Yan, C. and Song, X.D. (2016), "Effects of foam core density and face-sheet thickness on the mechanical properties of aluminum foam sandwich", *Steel Compos. Struct., Int. J.*, **21**(5), 1145-1156.
- Yan, C. and Song, X.D. (2017), "Bending behavior of aluminum foam sandwich with 304 stainless steel face-sheet", *Steel Compos. Struct., Int. J.*, **25**(3), 327-335.
- Yazdani Sarvestani, H., Mirkhalaf, M., Akbarzadeh, A.H., Backman, D., Genest, M., and Ashrafi, B. (2019), "Multilayered architected ceramic panels with weak interfaces: energy absorption and multi-hit capabilities", *Mater. Des.*, **167**, 107627.
- Yeganeh, E.M., Liaghat, G.H. and Pol, M.H. (2016), "Laminate composites behavior under quasi-static and high velocity perforation", *Steel Compos. Struct., Int. J.*, **22**(4), 777-796.
- Yin, H., Wen, G., Liu, Z. and Qing, Q. (2014), "Crashworthiness optimization design for foam-filled multi-cell thin-walled structures", *Thin-Wall. Struct.*, **75**(1), 8-17.
- Yurddaskal, M. and Okutan Baba, B. (2016), "The effect of curvature on the impact response of foam-based sandwich composite panels", *Steel Compos. Struct., Int. J.*, **20**(5), 983-997.
- Zhang, Z.H., Liu, S.T. and Tang, Z.L. (2010), "Crashworthiness investigation of kagome honeycomb sandwich cylindrical column under axial crushing loads", *Thin-Wall. Struct.*, **48**(1), 9-18.
- Zhang, Z.Y., Sun, W., Zhao, Y.S. and Hou, S.J. (2018), "Crashworthiness of different composite tubes by experiments and simulations", *Compos.: Part B*, **143**, 86-95.

CC